Research Article | Vol. 31, No. 15 / 17 Jul 2023 / Optics Express 24845
Optics EXPRESS

Sparse reconstruction based on dictionary learning and group structure strategy for cone-beam X-ray luminescence computed tomography

YI CHEN,[1,2] MENGFEI DU,[1,2] GEGE ZHANG,[1,2] JUN ZHANG,[1,2] KANG LI,[1,2,3] LINZHI SU,[1,2,4] FENGJUN ZHAO,[1,2] HUANGJIAN YI,[1,2] AND XIN CAO[1,2,5]

[1]*School of Information Science and Technology, Northwest University, Xi'an, Shaanxi 710127, China*
[2]*National and Local Joint Engineering Research Center for Cultural Heritage Digitization, Xi'an, Shaanxi 710127, China*
[3]*likang@nwu.edu.cn*
[4]*sulinzhi029@163.com*
[5]*xin_cao@163.com*

Abstract: As a dual-modal imaging technology that has emerged in recent years, cone-beam X-ray luminescence computed tomography (CB-XLCT) has exhibited promise as a tool for the early three-dimensional detection of tumors in small animals. However, due to the challenges imposed by the low absorption and high scattering of light in tissues, the CB-XLCT reconstruction problem is a severely ill-conditioned inverse problem, rendering it difficult to obtain satisfactory reconstruction results. In this study, a strategy that utilizes dictionary learning and group structure (DLGS) is proposed to achieve satisfactory CB-XLCT reconstruction performance. The group structure is employed to account for the clustering of nanophosphors in specific regions within the organism, which can enhance the interrelation of elements in the same group. Furthermore, the dictionary learning strategy is implemented to effectively capture sparse features. The performance of the proposed method was evaluated through numerical simulations and *in vivo* experiments. The experimental results demonstrate that the proposed method achieves superior reconstruction performance in terms of location accuracy, target shape, robustness, dual-source resolution, and *in vivo* practicability.

1. Introduction

X-ray luminescence computed tomography (XLCT) is a hybrid X-ray CT/optical imaging modality [1,2]. In XLCT, imaging probes, known as nanophosphors, are excited by X-ray beams to emit visible or near-infrared (NIR) light, which is then captured by photon detectors, resulting in a natural combination of high-resolution X-ray structural imaging with the high-sensitivity and high-specificity optical molecular imaging [3,4]. XLCT has been used in tumor imaging and treatment, for example, Hyeon et al. used XLCT for angiography and bimodal image-guided lymph node imaging [5]. J.Sailor et al. applied XLCT to breast cancer tumor imaging [6]. These preclinical studies will promote the clinical application of XLCT. Moreover, compared with other optical molecular imaging modalities such as bioluminescence tomography (BLT) [7,8] and fluorescence molecular tomography (FMT) [9,10], XLCT offers several advantages. Due to the high penetration and limited scattering of X-rays in biological tissue, XLCT can avoid background optical signals and autofluorescence [11,12].

In general, there are two primary types of XLCT systems based on the shape of the X-ray beam. One type is the pencil-beam XLCT (PB-XLCT) or narrow-beam XLCT (NB-XLCT) imaging

#493797 https://doi.org/10.1364/OE.493797
Journal © 2023 Received 25 Apr 2023; revised 11 Jun 2023; accepted 13 Jun 2023; published 12 Jul 2023

Optics EXPRESS

system, while the other is the cone-beam XLCT (CB-XLCT) [13]. However, although the first type of XLCT technique can achieve higher spatial resolution, its long data acquisition time makes it unsuitable for fast biomedical applications [14]. CB-XLCT, on the other hand, utilizes cone-beam geometry to cover the entire body simultaneously, eliminating the translation scanning process required in PB-XLCT and NB-XLCT, thereby speeding up the imaging and acquisition process [11]. Furthermore, CB-XLCT has the advantage of making full use of the X-ray dose compared to PB-XLCT [15]. Therefore, this study was only carried out using CB-XLCT.

However, due to the high scattering and low absorption of photons transmitted through biological tissues, CB-XLCT reconstruction is an ill-posed problem [3]. In addition, the inadequate external measurements also hinder the ability to obtain satisfactory reconstruction results [16]. To address these issues and improve the quality of reconstruction, several methods have been proposed by researchers in recent years. Zhang et al. proposed using a Bayesian method with a Gaussian Markov random field model to preserve target edges [17]. Considering that the distribution of nanophosphors *in vivo* is sparse, compressed sensing (CS) technology [18] can be adopted in the CB-XLCT reconstruction process, and L_1-norm as a convex relaxation of L_0-norm, which is often used to promote the sparsity of the solution [19]. Based on L_1-norm, a primal–dual Newton conjugate gradient method (pdNCG) was proposed by Gao et al. to alleviate ill-posedness [13]. There are also some hybrid regularization methods with L_1-norm proposed, for example, Zhang et al. proposed the joint L_1 and total variation regularization method (L_1-TV) [1] and Zhao et al. proposed an elastic net-L_1L_2 method based on the combination of the L_1 and L_2 regular terms for CB-XLCT reconstruction [3]. Moreover, with the help of CT images, group sparse priori is also used by Gao et al. to describe the relationship between elements [20]. In addition to sparse prior information, structural priori, optical properties, multi-spectral information and permission source regions have also been effectively used to improve reconstruction performance [9,21–23].

In this paper, a sparse reconstruction method based on dictionary learning and group structure (DLGS) strategy is proposed to improve the reconstruction quality of CB-XLCT. Most traditional convex or proximal convex optimization methods tend to neglect the spatial interdependence of relationships within the subspace after imposing a sparse constraint, leading to inaccurate spatial positioning and low morphological recovery. To address this issue, the fact that nanophosphors usually cluster in specific regions within the organism is considered during the reconstruction process. Specifically, DLGS groups adjacent nodes together, which strengthens the relationships between nodes within the group. In addition, dictionary learning (DL) aims to linearly represent redundant raw signals using sparse signals [24,25],effectively capturing important sparse features, and making it suitable for solving the problem of CB-XLCT reconstruction. To evaluate the reconstruction performance of our method, a series of numerical simulations and simulation experiments are performed and DLGS method was compared with the adaptive Tikhonov regularization algorithm with L_2-norm (Adaptik-L_2) [26], the orthogonal matching pursuit based on L_0-norm (OMP-L_0) [27], and the incomplete variables truncated conjugate gradient with L_1-norm (IVTCG-L_1) [28] in terms of location accuracy, target shape, robustness, dual-source resolution and *in vivo* practicability.

The structure of the remainder of this paper is organized as follows. In Section 2, a detailed description of the CB-XLCT imaging model and the proposed DLGS method is provided. In Section 3, detailed numerical simulations and *in vivo* experiments are conducted to evaluate the performance of the reconstruction method. In Section 4, the experimental results obtained using different reconstruction methods are summarized. Finally, in Section 5, the main findings of this work are discussed and concluded.

Optics EXPRESS

2. Methodology

2.1. Photon propagation model

In CB-XLCT, X-rays are emitted by cone-beam incoherent X-ray sources, which travel through biological tissues and excite nanophosphors to produce luminescence. According to Beer-Lambert's law, the X-ray intensity $X(r)$ along the primary path of the propagation process of X-ray in the tissue can be expressed as follows [29]:

$$X(r) = X(r_0)exp\left\{-\int_{r_0}^{r}\mu_x(\tau)d\tau\right\} \tag{1}$$

where $X(r_0)$ is the X-ray intensity (W cm^{-3}) at the initial position r_0, and $\mu_x(\tau)$ is the X-ray attenuation coefficient at position τ, which can be obtained from CT data. Sequentially, when the excitable nanophosphors emit visible or NIR light after irradiation, the source energy density $S(r)$ (W cm^{-3}) can be calculated as follows [15]:

$$S(r) = \Gamma X(r)n_c(r) \tag{2}$$

where Γ represents the light yield of nanoparticles (mg/mL), and $n_c(r)$ represents the concentration of nanophosphors at position r, respectively. The transportation process of visible light or NIR light in biological tissue can be modeled by the radiative transfer equation (RTE) [30], but it is challenging to solve RTE directly because of its high mathematical complexity. Due to the highly scattering and weak absorption properties of visible or NIR spectral window in biological tissue, in general, the RTE model can be simplified to the following steady-state diffusion equation (DE) model with Robin-type boundary condition, which is defined as follows [31,32]:

$$\begin{cases} -\nabla[D(r)\nabla\Phi(r)] + \mu_a(r)\Phi(r) = S(r) & (r \in \Omega) \\ \Phi(r) + 2\kappa D(r)[v\nabla\Phi(r)] = 0 & (r \in \partial\Omega) \end{cases} \tag{3}$$

where $D(r)$ is the diffusion coefficient, which can be calculated by $D(r) = [3(\mu_a(r) + \mu_s'(r))]^{-1}$, and $\mu_a(r)$ and $\mu_s'(r)$ are the absorption and reduced scattering coefficients at the position r, respectively. $\Phi(r)$ is the photon flux at position r, and Ω is the domain of the imaged object and $\partial\Omega$ is the boundary of Ω. κ is the boundary mismatch factor and v is the outward unit normal vector on the boundary $\partial\Omega$.

Based on the finite element method (FEM) [33], after the imaging domain is discretized, Eq. (3) can be rewritten into the following matrix equation:

$$K\Phi = F\rho \tag{4}$$

with

$$\begin{aligned} K_{ij} &= \int_\Omega (D(r)\nabla\psi_i(r)\nabla\psi_j(r) + \mu_a(r)\nabla\psi_i(r)\nabla\psi_j(r))dr + \frac{1}{2\kappa}\int_{\partial\Omega}\psi_i(r)\nabla\psi_j(r)dr \\ F_{ij} &= \int_\Omega \Phi(r)\psi_i(r)\psi_j(r)dr \end{aligned} \tag{5}$$

where ρ is the nanophosphors density to be reconstructed; K_{ij} and F_{ij} are the elements of matrix K and A, respectively; ψ_i and ψ_j denote the corresponding elements of the test function.

Since the matrix K is positive definite, Eq. (4) can be rewritten as

$$\Phi = A\rho \tag{6}$$

where $A = K^{-1}F$ is the weight matrix with size of $M \times N$, and Φ is the photon measurements vector on the object surface, and its size is $N \times 1$.

Optics EXPRESS

2.2. Reconstruction based on DLGS method

The distribution of unknown nanophosphors ρ is reconstructed using the visible or NIR measurement Φ captured by the highly sensitive electron multiplying charge coupled device (EMCCD) camera, which is the CB-XLCT imaging goal. However, due to the severe scattering of visible and NIR light in biological tissue, the system matrix A becomes ill-conditioned. As a result, it is impractical to solve Eq. (6) directly. Compared to the entire imaging object, the distribution of nanophosphors is small and sparse [34]. Inspired by CS theory, L_p regularization term can be applied to the objective function to obtain stable and robust solutions, as follows [35]:

$$min||A\rho - \Phi||_2^2 + \lambda||\rho||_p \tag{7}$$

where λ is the regularization parameter, and $||\rho||_p = \left(\sum_{i=1}^{N} |\rho_i|^p\right)^{1/p}$ is the L_p-norm of ρ. When $p = 0$, Eq. (7) becomes L_0 regularization problem which ensures the sparsest CB-XLCT reconstruction; When $p = 1$, Eq. (7) will be a L_1 regularization problem which approximates the L_0-norm, and if $p = 2$, Eq. (7) is a Tikhonov regularization and usually results in over-smoothed reconstruction. Since then, the CB-XLCT reconstruction problem is transformed into an optimization problem of ρ in Eq. (7). In this work, the $p = 0$ is adopted by us, and its constrained optimization form can be expressed as follows:

$$argmin||A\rho - \Phi||_2^2 \quad s.t. \quad ||\rho||_0 \leq K \tag{8}$$

where K is the sparsity level of the reconstruction result.

Inspired by DL strategy, the matrix A in CB-XLCT reconstruction can be viewed as a redundant dictionary and the vector ρ as its corresponding sparse coefficient. The DLGS strategy takes into account the group structure of nanophosphor distribution in organisms and consists of three main stages: grouping, sparse coding, and dictionary update. The orthogonal matching pursuit (OMP) algorithm [36] is adopted in the sparse coding stage for its fast convergence and high efficiency. The K-Singular value decomposition (K-SVD) algorithm [37], as an extension of the K-means algorithm, is used in the dictionary update stage for its efficient training. And the simple flowchart of DLGS strategy is summarized in Algorithm 1.

Algorithm 1: DLGS for CB-XLCT reconstruction

Input: system matrix A, photon measurement Φ, sparse level K.
Initialization: $\rho^0 = 0$, $k_{max} = 1000$, $err = 1e-6$, residual error vector $r^0 = \Phi$, current iteration $k = 1$, support set $S = \emptyset$.
Step 1: Tetrahedral mesh nodes are grouped into N groups, ρ and Φ are adjusted according to Eq. (9) and Eq. (10), respectively.
Step 2:
While $\|X^k - X^{k-1}\|_2 > err$ or $k < k_{max}$ do
1): Sparse coding stage
Update the corresponding row of the sparse representation ρ in the support set S through the Eq. (12), Eq. (13), Eq. (14), Eq. (15).
2): Dictionary update stage
Update the corresponding column of dictionary in the support set S through the Eq. (18), Eq. (19).
3): $k = k + 1$
End while
Output: $X = X^k$

Optics EXPRESS

2.2.1. Grouping stage

In this stage, the main task is to combine a node i with the nearest three nodes to form a group of G_i. In addition, the photon measurements vector Φ and reconstruction result vector ρ also need to be adjusted according to the node grouping results. The specific grouping information is as follows.

Under the FEM, the CB-XLCT imaging object is divided into a Cartesian mesh system. Tetrahedral mesh data, similar to graph structure, contains two types of data: nodes and tetrahedral node geometric information. It is necessary to integrate the tetrahedral geometry into the reconstruction method during CB-XLCT reconstruction. Based on the discrete tetrahedral mesh structure, four adjacent nodes are assigned to the same group to preserve the local spatial information. The reconstruction result ρ can then be reformulated as:

$$\rho = (\rho_{G_1}, \rho_{G_2}, \cdots \rho_{G_N})^T \tag{9}$$

where $G_i \subset \{1, 2, 3, \cdots N\}$ denotes the subscripts set of i-th group of nodes, ρ_{G_i} denotes the tetrahedron nodes under the same group G_i, and the size of ρ becomes $N \times N$. Similarly, surface photon measurement needs to be rewritten as:

$$\Phi = (\Phi_{G_1}, \Phi_{G_2}, \cdots \Phi_{G_N})^T \tag{10}$$

where Φ_{G_i} denotes the photon measurement of nodes under the same group G_i, and the size of Φ becomes $M \times N$. Therefore, in the following, both the reconstruction result ρ and the surface photon measurement Φ contain group structure.

2.2.2. Sparse coding stage

In this stage, the dimensions of the system matrix A, the surface photon measurement Φ and the reconstruction result vector ρ are consistent with the respective dimensions after the grouping stage.

The objective optimization function to be dealt with in the sparse coding stage can be expressed as follows:

$$\underset{\rho}{argmin}\, ||\Phi - A\rho||_2^2 \quad s.t. \quad ||\rho||_0 \leq K. \tag{11}$$

Finding a stable solution using traditional optimization methods is difficult because it is Np-hard. The OMP algorithm can be used as a greedy algorithm to find an approximate solution. An empty support set S_s is defined to contain the index of the selected column. In each iteration, after calculating the correlation between the column of matrix A_i and the residual matrix r^{k-1} with size of $M \times N$, the group with maximum correlation is selected into the support set S, expressed as follows:

$$\begin{aligned} s_k &= \underset{i}{argmax}\, ||A_i^T r^{k-1}||_1 \\ S &= S \cup s_k \end{aligned} \tag{12}$$

where k represents the current iteration. When the number of elements in the support set S meets the sparsity level, the iteration stops. The residual vector r can be calculated as follows:

$$r = \Phi - A\rho = \Phi - AA^+\Phi \tag{13}$$

where A^+ represents the pseudo-inverse of A, and its dimension is $N \times M$, which can be calculated as:

$$A^+ = (A^T A)^{-1} A^T \tag{14}$$

Optics EXPRESS

Consequently, based on Eq. (12), the residual vector in the current iteration k can be reformulated as follows:

$$r^k = \Phi - A_S A^+{}_S \Phi \tag{15}$$

where A_S and $A^+{}_S$ denote the system matrix and its pseudo-inverse in the support set S, respectively. Let L denotes the length of support set S, then the dimension of A_S is $M \times L$, and the dimension of $A^+{}_S$ is $L \times M$. Finally, the value of the element ρ_S corresponding to the subscript in the support set S is updated as follows:

$$\rho_S = A^+{}_S \Phi \tag{16}$$

It should be noted that the matrix ρ is initialized to 0, and only the rows corresponding to ρ in the support set are updated, and the updated results are saved in ρ_S.

2.2.3. Dictionary update stage

The K-SVD algorithm is used in the dictionary update stage, and the objective function that needs to be optimized becomes:

$$\underset{A}{argmin} \, ||\Phi - A\rho||_2^2 \quad s.t. \quad ||\rho||_0 \leq K. \tag{17}$$

The column of matrix A can be regarded as a set of atoms or basic vectors. Then Eq. (17) can be rewritten as:

$$\begin{aligned} \underset{A}{argmin} \, ||A\rho - \Phi||_2^2 &= \underset{A}{argmin} \left| |\Phi - \textstyle\sum_{j=1}^{N} A_j \rho_j^T \right| |_2^2 \\ &= \underset{A}{argmin} \left| |\left(\Phi - \textstyle\sum_{j \neq i}^{N} A_j \rho_j^T \right) - A_i \rho_i^T \right| |_2^2 \end{aligned} \tag{18}$$

where A_j represents the j-th column vector of dictionary A, and ρ_j^T represents the j-th row vector of sparse representation ρ. For the purpose of mathematical derivation, let $E = \left(\Phi - \sum_{j \neq k}^{N} A_j \rho_j^T \right)$ with size of $M \times N$ denotes an error matrix. The dictionary only updates the corresponding columns of ρ_S in the support set to ensure sparsity, then a new error matrix E^s is formed. Next, the error matrix E_S with size of $M \times L$ is decomposed by SVD as follows:

$$E_S = U \Lambda \mathrm{T} \tag{19}$$

where the dimensions of matrices U, Λ and T are $M \times M$, $M \times L$ and $L \times L$, respectively. Then, the i-th column of the dictionary is updated to $A_i = U(:, 1)$, where $U(:, 1)$ denotes the first column of U. When each column of the A_S is updated, the iteration stops.

3. Experiment design

In this section, several numerical simulations and *in vivo* experiment were designed to evaluate the proposed method. Three existing algorithms: Adaptik-L_2, OMP-L_0, and IVTCG-L_1 were used for comparison in terms of location accuracy, morphological recovery, robustness, and *in vivo* practicability. All experiments and programs were executed on a laptop with an AMD Ryzen 7 5800 H CPU (3.20 GHz) and 16GB RAM.

3.1. Evaluation indexes

To further quantify the performance of different methods in CB-XLCT reconstruction, three evaluation indexes were adopted: position error (PE) [38], Dice similarity coefficient (DICE) [39], and relative quantity error (RQE) [40].

Optics EXPRESS

PE was used to evaluate spatial positioning accuracy by calculating the Euclidean distance between the reconstructed region center coordinates (x_r, y_r, z_r) and the actual region center coordinates (x_a, y_a, z_a):

$$PE = \sqrt{(x_r - x_a)^2 + (y_r - y_a)^2 + (y_r - y_a)^2} \tag{20}$$

DICE is applied to assess morphological recovery between the reconstructed target region R_r and the real target region R_a:

$$DICE = \frac{2|R_r \cap R_a|}{|R_r| + |R_a|} \tag{21}$$

The value of DICE ranged from 0 to 1. The greater the DICE value, the more overlap between the reconstructed target region and the real target region, indicating a higher degree of morphological recovery.

RQE is adopted to assess intensity recovery between the reconstructed target region and the real target region:

$$RQE = \frac{|RD_r - RD_a|}{RD_a} \tag{22}$$

where RD_r and RD_a are the reconstructed target density and the actual target density. The closer the RQE is to 0, the closer the density of the reconstructed target is to that of the actual target.

3.2. Numerical simulation setup

A heterogeneous cylindrical phantom with a height of 30 mm and a radius of 10 mm was used for simulation. It consists of five main organs: muscle, bone, heart, liver, and lungs, as shown in Fig. 1(a). According to the work of Tian et al. [41], the optical properties of these five organs at a wavelength of 650 nm were listed in Table 1.

Table 1. Optical properties of the heterogeneous cylindrical phantom at 650 nm

Tissue	$\mu_a(r)[mm^{-1}]$	$\mu_s(r)[mm^{-1}]$	g
Muscle	0.010	4.000	0.900
Bone	0.002	20.000	0.900
Heart	0.200	16.000	0.850
Liver	0.035	6.000	0.900
Lungs	0.350	23.000	0.900

In the cylindrical phantom, the single-target is a sphere with a radius of 1 mm located at (0.0, -4.0, 18.0) mm to simulate early tumors, as shown in Fig. 1(b). The dual-target consists of two identical spheres with a radius of 1 mm located at (-3.0, -6.0, 6.0) mm and (-3.0, 0.0, 6.0) mm, respectively, as shown in Fig. 1(c). In the anti-noise experiment, based on the single-target experiment, Gaussian noise of 5%, 10%, 15%, 20% and 25% was added in turn and reconstruction results of different methods under different Gaussian noise ratios were observed.

The attenuation coefficient of X-ray was set to 0.0535 mm^{-1} and the voltage and current of the cone-beam X-ray source were set to 50 KVp and 1 mA, respectively. The cylinder model was rotated 360° and luminescent images were collected every 90°for reconstruction, resulting in total of 4 projections.

The cylinder model was discretized into a tetrahedral mesh model with 4626 nodes and 25840 tetrahedral elements using COMSOL Multiphysics 5.6 (COMSOL, Inc., Burlington, Massachusetts) software [42], the mean element edge size is 1.37 mm, as shown in Fig. 1 (b). The forward simulation results of single-target and dual-target can be obtained using the Monte Carlo (MC) method implemented by molecular optical simulation environment (MOSE, Version 2.3) software [43], as shown in Fig. 1 (e) and Fig. 1(f).

Optics EXPRESS

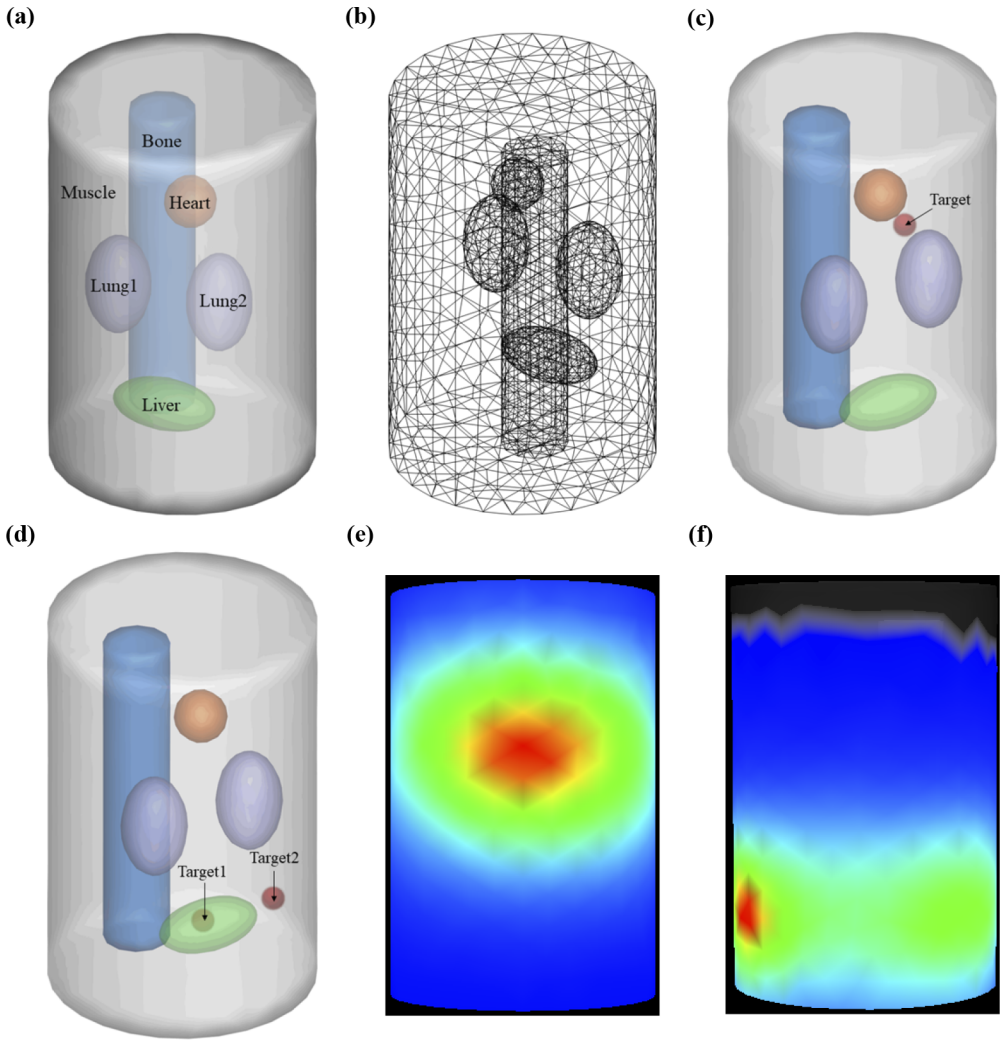

Fig. 1. Heterogeneous cylindrical phantom for numerical simulation studies: (a) The 3D view of the main organs of cylindrical phantom. (b) The 3D view of meshed biological tissues. (c) Cylindrical phantom with single-target. (d) Cylindrical phantom with dual-target. (e) Forward simulation of cylindrical phantom with single-target. (f) Forward simulation of cylindrical phantom with dual-target.

3.3. Implanted experiment

To ensure the feasibility of the proposed method for *in vivo* CB-XLCT, data was collected from an eight-week-old BALB/C nude female mouse was collected using an XLCT imaging system. All experimental procedures are under the approval of the Animal Ethics Committee of the Northwest University of China. In detail, a flexible plastic tube with a radius of 1 mm and a height of 2 mm containing Gd_2O_2S:Tb nanophosphors (about 20 μl), which was used to simulate an early tumor. The homogeneous absorption coefficient and reduced scattering coefficient were set to 0.3 mm^{-1} and 10 mm^{-1}, respectively. The imaging system included a cone beam X-ray source (Apogee, Oxford Instruments, USA), a CMOS X-ray detector panel (C7921CA-02, Hamamatsu, Japan), an electron-multiplying CCD (EMCCD) camera (PIXIS 2048, Princeton Instruments,

Optics EXPRESS

USA) and a rotation stage, as shown in Fig. 2. In detail, the X-ray source excited nanophosphors in biological tissue with a voltage and current of 50KVp and 1 mA, respectively. The CMOS X-ray detector panel had a pixel size of 50 μm, which was used to detect transmitted X-rays, and then obtained high-resolution CT imaging. The EMCCD with a micro 55-mm f/2.8 lens (Nikkor, Nikon, Japan) was placed perpendicular to the X-ray source to capture the optical data at a wavelength of 620 nm with an integration time and binning of 30 s and 2×2, respectively. The mouse was fixed on the rotation stage and rotated 360° at 1° intervals to obtain both micro-CT images and the X-ray projection images.

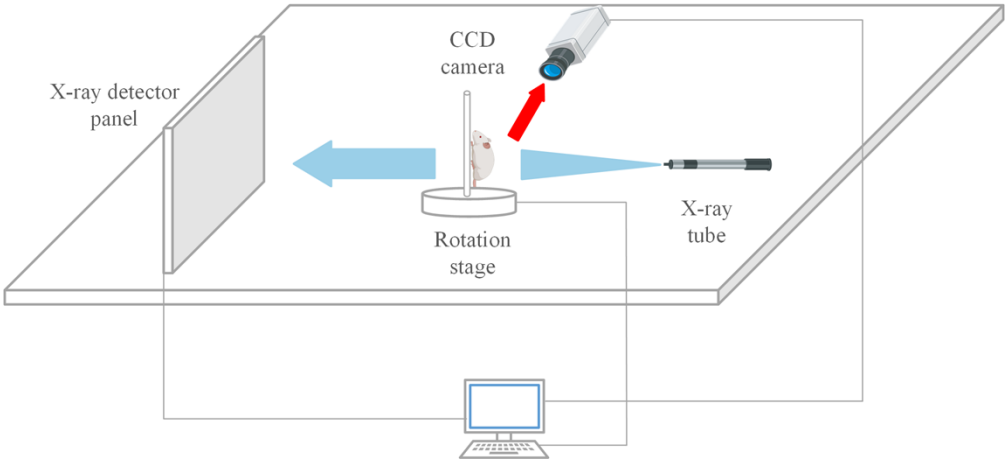

Fig. 2. The schematic diagram of the CB-XLCT system.

After collecting the 3D volume data, the Feldkamp–Davis–Kress (FDK) method [44] was used to perform 3D reconstruction of the XCT projections. The forward measurement of nanophosphors was then mapped onto the surface. The nanophosphors target was implanted into the abdomen of the mouse at the coordinates (11.5, 6.5, 15.1) mm. For the inverse reconstruction, the mesh of the *in vivo* experiment was discretized into 6061 nodes and 27776 tetrahedral elements.

4. Results

4.1. Numerical simulations results

4.1.1. Single-target experiment

The reconstruction results of the single-target experiment were shown in Fig. 3. The first row displayed the 3D view of the reconstruction results of Adaptik-L_2, OMP-L_0, IVTCG-L_1, and DLGS methods, where the dark red region indicated the 3D distribution of the nanophosphors target. The second row showed the cross-section view of the single target reconstruction result by different methods at the $Z = 1$ mm plane, with the white circle representing the actual location and edge of the real target. Additionally, the quantitative evaluation results of the four reconstruction methods were summarized in Table 2.

It is obvious that, compared with the other three methods, the reconstruction result of DLGS is closest to the actual target region in terms of location accuracy and morphological recovery. Meanwhile, DLGS has a lower RQE, as shown in Table 2, indicating that DLGS performs well in terms of density recovery.

Optics EXPRESS

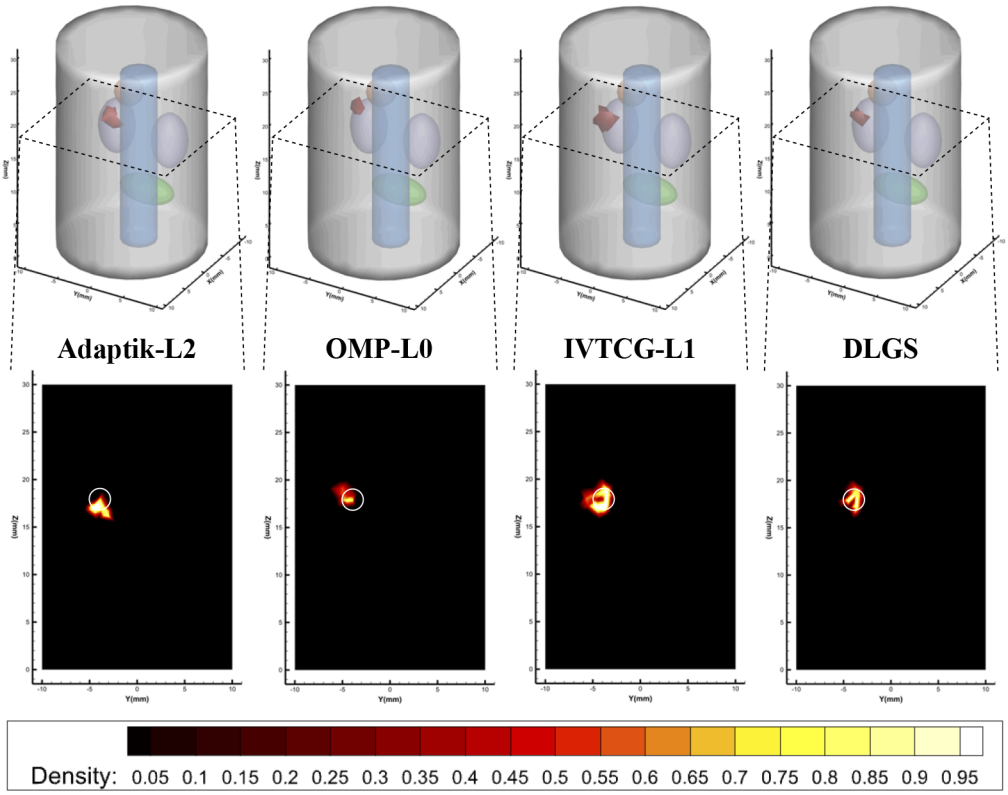

Fig. 3. Reconstruction results of four methods for a single spherical target.

Table 2. Quantitative results of different methods in single-target reconstruction experiment.

Method	Reconstructed region center (mm)	PE (mm)	DICE	RQE
Adaptik-L_2	(-1.145, -3.758, 17.867)	1.178	0.427	0.765
OMP-L_0	(-0.671. -4.404, 18.367)	0.865	0.553	0.271
IVTCG-L_1	(0.597, -4.286, 18.052)	0.663	0.625	1.269
DLGS	(0.356, -3.941, 17.969)	0.362	0.821	0.446

4.1.2. Dual-target experiment

Fig. 4 showed the results of the dual-target simulation experiment, with each row corresponding to the axial view, coronal view, sagittal view (two sheets)**,** and 3D view of the reconstruction results of the Adaptik-L_2 method, OMP-L_0 method, IVTCG-L_1 method, and DLGS method. The reconstructed and actual targets were represented in the same way as in single-target experiment. The edge-to-edge distance between the two targets was 4 mm. Through Fig. 4, it can be found that the location accuracy and spatial overlap degree of the Adaptik-L_2 method and OMP-L_0 method were poor, while IVTCG performed better than these two methods but the reconstruction performance by DLGS method was the best. Table 3 confirmed our conclusion with its quantitative results showing that the result by DLGS had the lowest PE and RQE and the highest DICE.

Optics EXPRESS

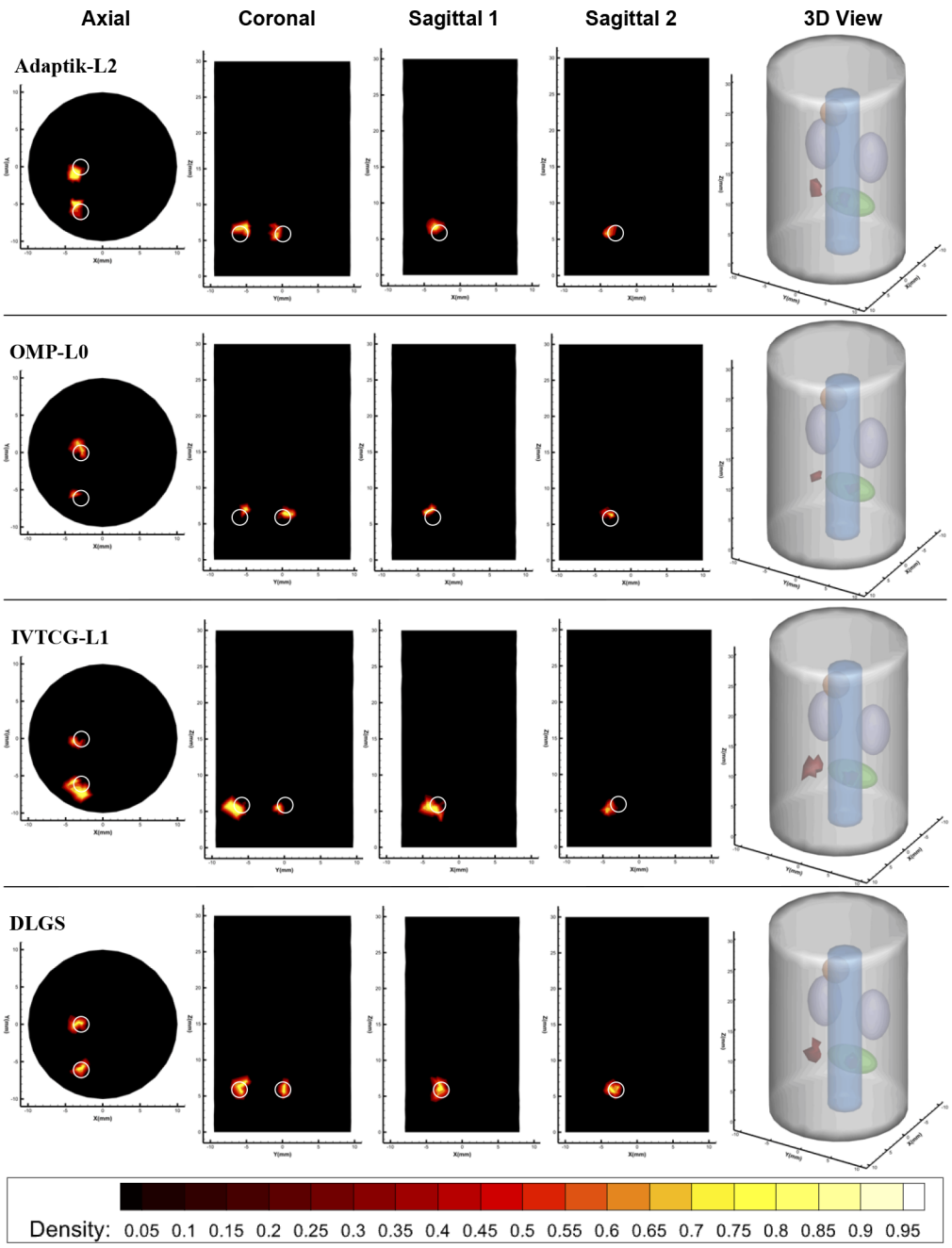

Fig. 4. Reconstruction results of four methods for dual-target.

Optics EXPRESS

Table 3. Quantitative results of different methods in dual-target reconstruction experiment.

Method	Reconstructed region center (mm)	PE (mm)	DICE	RQE
Adaptik-L_2	(-3.503, -5.500,6.823)	1.086	0.522	0.383
	(-3.587, -1.165, 6.630)	1.448	0.494	1.101
OMP-L_0	(-3.597, -5.208, 6.641)	1.181	0.433	0.531
	(-3.161, 0.630, 6.461)	0.797	0.400	0.319
IVTCG-L_1	(-2.866, -6.626, 5.294)	0.953	0.609	0.878
	(-3.541, -0.573, 5.451)	0.960	0.432	0.382
DLGS	(-2.962, -5.656, 6.489)	0.599	0.852	0.205
	(-3.510, 0.115, 6.040)	0.524	0.647	0.348

4.1.3. Anti-noise experiment

The experimental results of anti-noise performance were shown in Fig. 5. Based on the single-target experiment, Gaussian noise was added to the measurement data at ratios of 5%, 10%, 15%, 20%, and 25%. Obviously, it can be observed that even as the Gaussian-noise ratio increased, the reconstruction performance of DLGS method did not deteriorate and even improved in some cases. These experimental results demonstrated that the DLGS method was robust when applied to CB-XLCT reconstruction, maintaining its performance even in the presence of significant noise.

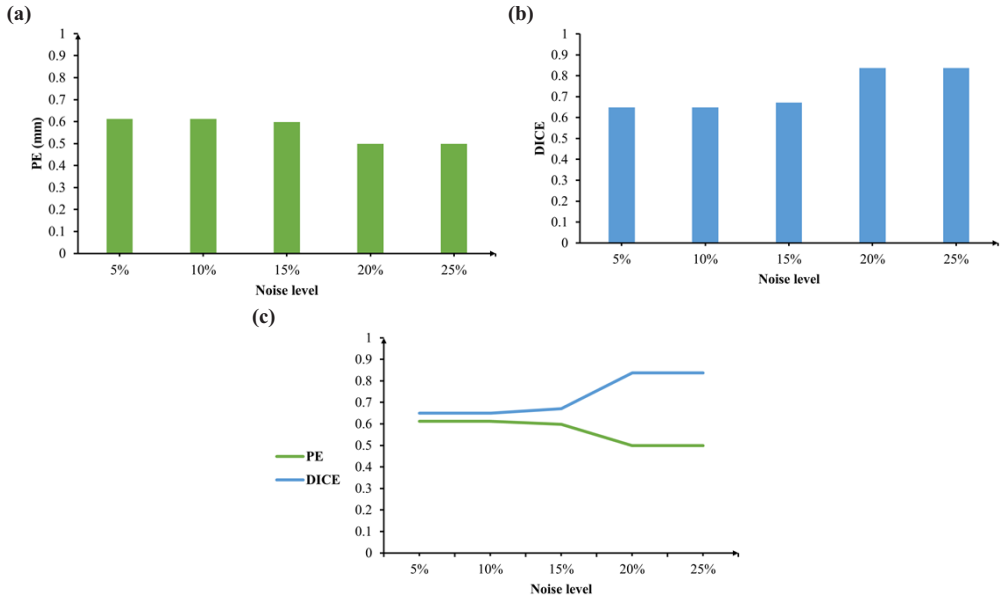

Fig. 5. (a) Illustration of PE at different noise levels. (b) Illustration of DICE at different noise levels. (c) The changes of PE and DICE at different noise levels.

4.2. *In vivo* experiment results

The results of the *in vivo* experiment were shown in Fig. 6. In the 3D view, the reconstructed area was represented in red. The cross view at the plane Z = 15.1 mm was also shown next to it. At the same time, for quantitative analysis of the reconstruction results by different methods, PE and DICE were calculated and summarized in Table 4.

Optics EXPRESS

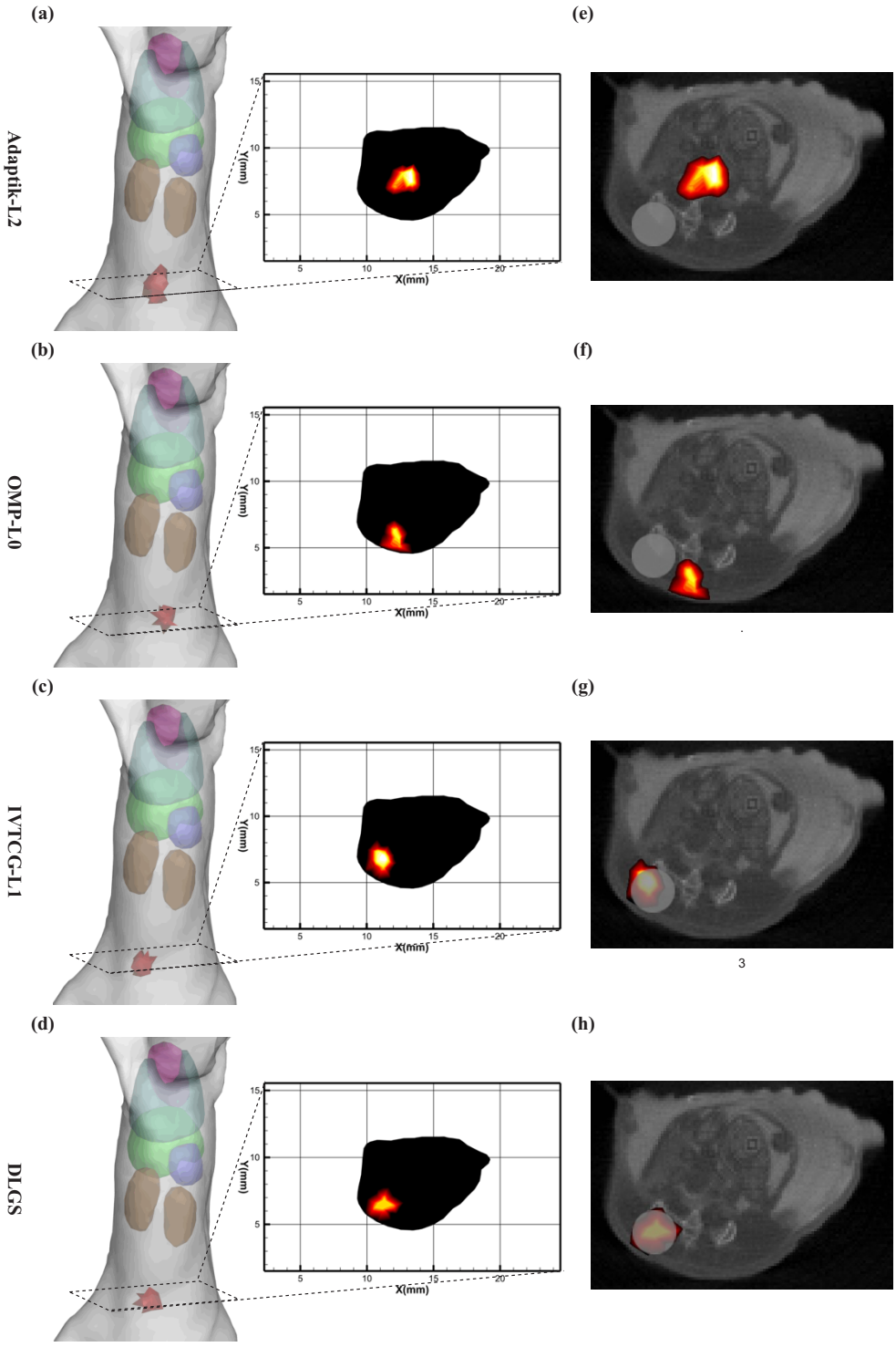

Fig. 6. Reconstruction results of the *in vivo* experiment. (a)-(d) 3D-view and transverse view of *in vivo* experiment result. (e)-(h) Images fused by the transverse view and CT image. The red area is the reconstruction result, and the gray-white circular area represents the section of the real source.

Optics EXPRESS

Table 4. Quantitative results of *in vivo* experiment.

Method	Reconstructed region center (mm)	PE (mm)	DICE
Adaptik-L_2	(12.842, 7.572, 14.592)	1.791	0.176
OMP-L_0	(12.215. 5.827, 15.708)	1.155	0.335
IVTCG-L_1	(11.303, 6.833, 14.708)	0.551	0.685
DLGS	(11.198, 6.509, 14.843)	0.397	0.802

According to the reconstruction results obtained by various methods, it was found that in terms of location accuracy, the PE of the reconstruction result obtained by Adaptik-L_2 and OMP-L_0 were 1.791 mm and 1.115 mm respectively. These values indicate a significant discrepancy between the reconstructed source center and the actual location, which is also confirmed by examining their cross-section. The PE of the reconstruction result obtained by IVTCG-L_1 method was 0.551, showing a small center error between the reconstruction result and the real source. However, the PE of reconstruction result of DLGS method was the lowest at 0.397, making it the most accurate of the four methods. In terms of morphological recovery, Adaptik-L_2 and OMP-L_0 also performed poorly with DICE values of 0.176 and 0.335, respectively. Compared with these two methods, IVTCG-L_1 had a higher degree of morphological recovery. However, among the four reconstruction methods, the reconstruction results by DLGS method had the highest DICE value at 0.802, indicating that the spatial overlap between its reconstruction results and the real source was also the highest, that is, its morphological recovery was more accurate.

5. Discussion and conclusion

CB-XLCT is a powerful hybrid imaging technique that provides unique imaging advantages. However, the reconstruction process for CB-XLCT is ill-posed, resulting in inferior image quality. To address this issue and improve the reconstructed quality, we proposed a reconstruction method named DLGS in this work. This method incorporates some specific prior knowledge, such as sparse priors and group structure, to alleviate the ill-posedness of the inverse problem. Due to the small and sparse distribution of nanophosphors in the body compared to the overall imaging object, and the tendency of nanophosphors to cluster together, it is reasonable to create an internal connection between adjacent nodes base on FEM. Hence, the group structure is considered to be used to enhance this internal relationship. The DLGS method is based on the DL approach and uses sparse approximation to establish an adaptive basis for specific imaging instances, preserving desirable features. The DLGS mainly consist of three stages: grouping, sparse coding, and dictionary learning. The last two stages are solved iteratively using the OMP algorithm and K-SVD algorithm. The OMP algorithm ensures stable convergence speed, while the K-SVD algorithm requires less computation and provides better reduction effects.

To evaluate the performance of our proposed DLGS method, several groups of numerical simulations and one group of *in vivo* experiment were designed and carried out. We employed three typical reconstruction methods, namely Adaptik-L_2, OMP-L_0, IVTCG-L_1, based on L_2-norm, L_0-norm, and L_1-norm respectively, to quantitively compare with our DLGS method. In the single-target simulation and dual-target simulation, as seen in Figs. 3 and 4, the reconstructed regions using the comparison methods exhibited some problems such as inaccurate location, over-sparse, over-smoothing. In contrast, our proposed method greatly overcame these problems, which is also verified by the results of quantitative analysis. In single-target reconstruction, our proposed DLGS method has the lowest PE of 0.362 and the highest DICE of 0.821. These results indicate that DLGS offers improved accuracy and better shape recovery compared to the other methods in CB-XLCT for single-target reconstruction. For dual-target reconstruction, DLGS shows similar performance to single-target reconstruction, with the lowest PE and the largest

Optics EXPRESS

DICE, suggesting that DLGS exhibits stronger dual-source reconstruction capabilities compared to the other three methods. In the anti-noise experiment, where different proportions of Gaussian noise (5%, 10%, 15%, 20%, 25%) were added, as observed in Fig. 5, the reconstruction results obtained by our proposed DLGS method demonstrate minimal fluctuations. The evaluation indexes show a PE range of 0.5 to 0.6 and a DICE range of 0.6 to 0.7, indicating the robustness of DLGS to noise in the reconstruction process. *In vivo* experiment was conducted to further verify the practicality of DLGS for FMT reconstruction in a real environment. As shown in Fig. 6 and the quantitative analysis listed in Table 4, the *in vivo* single-target experimental results showed that the reconstructed area obtained by DLGS was a better approximation of the real region than that obtained by other traditional method used for comparison, and the specific quantization result is $PE = 0.379\ mm$ and $DICE = 0.802$, which is superior to the other three reconstruction methods. In summary, the simulation experiments and *in vivo* experiments consistently demonstrate that DLGS outperforms the other methods in terms of localization accuracy and morphological recovery. The reconstruction performance of IVTCG-L_1, is ranked second, while the reconstruction performance of Adaptik-L_2 and OMP-L_0 exhibit less satisfactory results.

However, it should be noted that there are still a few challenges need to be addressed. Firstly, the value of sparsity K needs to be determined manually and cannot be adjusted automatically. Secondly, the DLGS method needs to be further validated in other optical tomography modalities to assess its effectiveness and generalizability. In addition, the attenuation coefficient obtained from CT data is not necessarily accurate for complex imaging samples, and in addition to the attenuation coefficient, the diffraction coefficient also has a certain influence on the intensity of X-ray computed tomography. Therefore, in our future work, we will focus on developing an adaptive sparsity adjustment scheme to address the first issue, and evaluate the performance of DLGS in other optical tomography techniques, such as Cerenkov luminescence tomography (CLT) [45–47], BLT, FMT, to investigate its potential utility in different imaging scenarios. Then we will find a method to correct attenuation coefficient in complex environment. For example, Feng et al. add the attenuation maps in the contribution value of the pixel in the X-ray fluorescence computed tomography (XFCT) reconstruction process to correct the attenuation coefficient [48]. Moreover, we will analyze the influence of diffraction coefficient.

In summary, we proposed a method based on dictionary learning and group structure to improve the accuracy of CB-XLCT reconstruction. The DL strategy is employed to address the ill-posedness of the system matrix and account for the sparsity of the nanophosphors targets, while the group structure is utilized to fully consider the internal relationship between nodes. Experimental results demonstrate that the DLGS method outperform other typical regularization-based methods, providing superior reconstruction quality in terms of location, morphology, and intensity. We believe that our proposed method will be beneficial for various preclinical applications of CB-XLCT.

Funding. National Natural Science Foundation of China (61701403, 61806164); Key Research and Development Program of Shaanxi Province (2019GY215, 2021ZDLSF06-04); China Postdoctoral Science Foundation (2018M643719); Graduate Innovation Program of Northwest University (CX2023185).

Disclosures. The authors declare no conflicts of interest.

Data availability. Data underlying the results presented in this paper are not publicly available at this time but may be obtained from the authors upon request.

References

1. T. Liu, J. Rong, P. Gao, H. Pu, W. Zhang, X. Zhang, Z. Liang, and H. Lu, "Regularized reconstruction based on joint L 1 and total variation for sparse-view cone-beam x-ray luminescence computed tomography," Biomed. Opt. Express **10**(1), 1–17 (2019).
2. G. Pratx, C. M. Carpenter, C. Sun, and L. Xing, "X-ray luminescence computed tomography via selective excitation: a feasibility study," IEEE Trans. Med. Imaging **29**(12), 1992–1999 (2010).

Optics EXPRESS

3. J. Zhao, H. Guo, J. Yu, H. Yi, Y. Hou, and X. He, "A robust elastic net-l1l2reconstruction method for x-ray luminescence computed tomography," Phys. Med. Biol. **66**(19), 195005 (2021).
4. H. Zhang, X. Huang, M. Zhou, G. Geng, and X. He, "Adaptive shrinking reconstruction framework for cone-beam X-ray luminescence computed tomography," Biomed. Opt. Express **11**(7), 3717–3732 (2020).
5. M. H. Oh, N. Lee, H. Kim, S. P. Park, Y. Piao, J. Lee, S. W. Jun, W. K. Moon, S. H. Choi, and T. Hyeon, "Large-scale synthesis of bioinert tantalum oxide nanoparticles for X-ray computed tomography imaging and bimodal image-guided sentinel lymph node mapping," J. Am. Chem. Soc. **133**(14), 5508–5515 (2011).
6. J. M. Kinsella, R. E. Jimenez, P. P. Karmali, A. M. Rush, V. R. Kotamraju, N. C. Gianneschi, E. Ruoslahti, D. Stupack, and M. J. Sailor, "X-ray computed tomography imaging of breast cancer by using targeted peptide-labeled bismuth sulfide nanoparticles," Angew. Chem. Int. Ed. **50**(51), 12308–12311 (2011).
7. Y. Chen, M. Du, W. Li, L. Su, H. Yi, F. Zhao, K. Li, L. Wang, and X. Cao, "ABPO-TVSCAD: alternating Bregman proximity operators approach based on TVSCAD regularization for bioluminescence tomography," Phys. Med. Biol. **67**(21), 215013 (2022).
8. H. Guo, J. Yu, Z. Hu, H. Yi, Y. Hou, and X. He, "A hybrid clustering algorithm for multiple-source resolving in bioluminescence tomography," J. Biophotonics **11**(4), e201700056 (2018).
9. Z. Hu, C. Fang, B. Li, Z. Zhang, C. Cao, M. Cai, S. Su, X. Sun, X. Shi, and C. Li, "First-in-human liver-tumour surgery guided by multispectral fluorescence imaging in the visible and near-infrared-I/II windows," Nat. Biomed. Eng. **4**(3), 259–271 (2019).
10. Z. Hu, Y. Qu, K. Wang, X. Zhang, J. Zha, T. Song, C. Bao, H. Liu, Z. Wang, and J. Wang, "In vivo nanoparticle-mediated radiopharmaceutical-excited fluorescence molecular imaging," Nat. Commun. **6**(1), 7560 (2015).
11. H. Zhang, L. Hai, J. Kou, Y. Hou, X. He, M. Zhou, and G. Geng, "OPK_SNCA: Optimized prior knowledge via sparse non-convex approach for cone-beam X-ray luminescence computed tomography imaging," Computer Methods and Programs in Biomedicine **215**, 106645 (2022).
12. H. Guo, H. Zhao, J. Yu, X. He, X. He, and X. Song, "X-ray luminescence computed tomography using a hybrid proton propagation model and Lasso-LSQR algorithm," J. Biophotonics **14**, e202100089 (2021).
13. P. Gao, K. Cheng, E. Schuler, M. Jia, W. Zhao, and L. Xing, "Restarted primal-dual Newton conjugate gradient method for enhanced spatial resolution of reconstructed cone-beam x-ray luminescence computed tomography images," Phys. Med. Biol. **65**(13), 135008 (2020).
14. H. Zhang, G. Geng, Y. Chen, F. Zhao, Y. Hou, H. Yi, S. Zhang, J. Yu, and X. He, "Performance evaluation of the simplified spherical harmonics approximation for cone-beam x-ray luminescence computed tomography imaging," J. Innov. Opt. Health Sci. **10**(03), 1750005 (2017).
15. D. Chen, S. Zhu, H. Yi, X. Zhang, D. Chen, J. Liang, and J. Tian, "Cone beam x-ray luminescence computed tomography: A feasibility study," Med. Phys. **40**(3), 031111 (2013).
16. P. Gao, J. Rong, H. Pu, T. Liu, W. Zhang, X. Zhang, and H. Lu, "Sparse view cone beam x-ray luminescence tomography based on truncated singular value decomposition," Opt. Express **26**(18), 23233–23250 (2018).
17. G. Zhang, F. Liu, J. Liu, J. Luo, Y. Xie, J. Bai, and L. Xing, "Cone beam x-ray luminescence computed tomography based on Bayesian method," IEEE Trans. Med. Imaging **36**(1), 225–235 (2017).
18. H. Pu, P. Gao, Y. Liu, J. Rong, F. Shi, and H. Lu, "Principal component analysis based dynamic cone beam x-ray luminescence computed tomography: a feasibility study," IEEE Trans. Med. Imaging **38**(12), 2891–2902 (2019).
19. S. Tzoumas, D. Vernekohl, and L. Xing, "Coded-aperture compressed sensing x-ray luminescence tomography," IEEE Trans. Biomed. Eng. **65**(8), 1892–1895 (2018).
20. P. Gao, J. Rong, T. Liu, W. Zhang, B. Lan, X. Ouyang, and H. Lu, "Limited view cone-beam x-ray luminescence tomography based on depth compensation and group sparsity prior," J. Biomed. Opt. **25**(01), 1–016004 (2020).
21. Y. Tan and H. Jiang, "DOT guided fluorescence molecular tomography of arbitrarily shaped objects," Med. Phys. **35**(12), 5703–5707 (2008).
22. Z. Hu, M. Zhao, Y. Qu, X. Zhang, M. Zhang, M. Liu, H. Guo, Z. Zhang, J. Wang, and W. Yang, "In vivo 3-dimensional radiopharmaceutical-excited fluorescence tomography," Journal of Nuclear Medicine **58**(1), 169–174 (2017).
23. J. Shi, F. Liu, J. Zhang, J. Luo, and J. Bai, "Fluorescence molecular tomography reconstruction via discrete cosine transform-based regularization," J. Biomed. Opt **20**(5), 055004 (2015).
24. X. Chen, Z. Du, J. Li, X. Li, and H. Zhang, "Compressed sensing based on dictionary learning for extracting impulse components," Signal Processing **96**, 94–109 (2014).
25. H. Su, F. Xing, and L. Yang, "Robust cell detection of histopathological brain tumor images using sparse reconstruction and adaptive dictionary selection," IEEE Trans. Med. Imaging **35**(6), 1575–1586 (2016).
26. X. Cao, B. Zhang, X. Wang, F. Liu, K. Liu, J. Luo, and J. Bai, "An adaptive Tikhonov regularization method for fluorescence molecular tomography," Med. Biol. Eng. Comput. **51**(8), 849–858 (2013).
27. J. Wang and B. Shim, "On the recovery limit of sparse signals using orthogonal matching pursuit," IEEE Trans. Signal Process. **60**(9), 4973–4976 (2012).
28. X. He, J. Liang, X. Wang, J. Yu, X. Qu, X. Wang, Y. Hou, D. Chen, F. Liu, and J. Tian, "Sparse reconstruction for quantitative bioluminescence tomography based on the incomplete variables truncated conjugate gradient method," Opt. Express **18**(24), 24825–24841 (2010).
29. X. Liu, Q. Liao, and H. Wang, "Fast x-ray luminescence computed tomography imaging," IEEE Trans. Biomed. Eng. **61**(6), 1621–1627 (2014).

Optics EXPRESS

30. Q. Zhang, H. Zhao, D. Chen, X. Qu, X. Chen, X. He, W. Li, Z. Hu, J. Liu, and J. Liang, "Source sparsity based primal-dual interior-point method for three-dimensional bioluminescence tomography," Opt. Commun. **284**(24), 5871–5876 (2011).
31. A. D. Klosea, B. J. Beattieb, H. Dehghanic, L. Vider, C. Le, V. Ponomarev, and R. Blasberg, "In vivo bioluminescence tomography with a blocking-off finite-difference SP 3 method and MRI/CT coregistration," Med. Phys. **37**(1), 329–338 (2009).
32. A. D. Klose and E. W. Larsen, "Light transport in biological tissue based on the simplified spherical harmonics equations," J. Comput. Phys. **220**(1), 441–470 (2006).
33. M. Schweiger, S. Arridge, M. Hiraoka, and D. Delpy, "The finite element method for the propagation of light in scattering media: boundary and source conditions," Med. Phys. **22**(11), 1779–1792 (1995).
34. X. Liu, X. Tang, Y. Shu, L. Zhao, Y. Liu, and T. Zhou, "Single-view cone-beam x-ray luminescence optical tomography based on Group_YALL1 method," Phys. Med. Biol. **64**(10), 105004 (2019).
35. H. Zhang, G. Geng, S. Zhang, K. Li, C. Liu, Y. Hou, and X. He, "Sparse non-convex lp regularization for cone-beam x-ray luminescence computed tomography," J. Mod. Opt. **65**(20), 2278–2289 (2018).
36. L. Denis, D. A. Lorenz, and D. Trede, "Greedy solution of ill-posed problems: error bounds and exact inversion," Inverse Problems **25**(11), 115017 (2009).
37. M. Aharon, M. Elad, and A. Bruckstein, "K-SVD: An algorithm for designing overcomplete dictionaries for sparse representation," IEEE Trans. Signal Process. **54**(11), 4311–4322 (2006).
38. Y. An, J. Liu, G. Zhang, J. Ye, Y. Du, Y. Mao, C. Chi, and J. Tian, "A novel region reconstruction method for fluorescence molecular tomography," IEEE Trans. Biomed. Eng. **62**(7), 1818–1826 (2015).
39. Y. Chen, W. Li, M. Du, L. Su, H. Yi, F. Zhao, K. Li, L. Wang, and X. Cao, "Elastic net-based non-negative iterative three-operator splitting strategy for Cerenkov luminescence tomography," Opt. Express **30**(20), 35282–35299 (2022).
40. D. Chen, S. Zhu, X. Chen, T. Chao, X. Cao, F. Zhao, L. Huang, and J. Liang, "Quantitative cone beam X-ray luminescence tomography/X-ray computed tomography imaging," Appl. Phys. Lett. **105**(19), 191104 (2014).
41. R. Han, J. Liang, X. Qu, Y. Hou, N. Ren, J. Mao, and J. Tian, "A source reconstruction algorithm based on adaptive hp-FEM for bioluminescence tomography," Opt. Express **17**(17), 14481–14494 (2009).
42. E. J. Dickinson, H. Ekström, and E. Fontes, "COMSOL Multiphysics®: Finite element software for electrochemical analysis. A mini-review," Electrochem. Commun. **40**, 71–74 (2014).
43. H. Li, J. Tian, F. Zhu, W. Cong, L. V. Wang, E. A. Hoffman, and G. Wang, "A mouse optical simulation environment (MOSE) to investigate bioluminescent phenomena in the living mouse with the monte carlo method1," Academic Radiology **11**(9), 1029–1038 (2004).
44. L. A. Feldkamp, L. C. Davis, and J. W. Kress, "Practical cone-beam algorithm," J. Opt. Soc. Am. A **1**(6), 612–619 (1984).
45. X. Cao, X. Wei, F. Yan, L. Wang, and X. He, "A Novel Stacked Denoising Autoencoder-Based Reconstruction Framework for Cerenkov Luminescence Tomography," IEEE Access **7**, 85178–85189 (2019).
46. W. Yang, W. Qin, Z. Hu, Y. Suo, R. Zhao, X. Ma, W. Ma, T. Wang, J. Liang, and J. Tian, "Comparison of Cerenkov luminescence imaging (CLI) and gamma camera imaging for visualization of let-7 expression in lung adenocarcinoma A549 Cells," Nucl. Med. Biol. **39**(7), 948–953 (2012).
47. Z. Hu, J. Liang, W. Yang, W. Fan, C. Li, X. Ma, X. Chen, X. Ma, X. Li, and X. Qu, "Experimental Cerenkov luminescence tomography of the mouse model with SPECT imaging validation," Opt. Express **18**(24), 24441 (2010).
48. L. Liu, Y. Huang, Q. Xu, L.-T. Yan, L. Li, S.-L. Feng, and X.-Q. Feng, "Attenuation correction of L-shell X-ray fluorescence computed tomography imaging," Chinese Phys. C **39**(3), 038203 (2015).